applied sciences

MDPI

Article

Long-Distance Measurements Using a Chromatic Confocal Sensor

Kiril Ivanov Kurtev [1,2,*], Juan Manuel Trujillo-Sevilla [1] and José Manuel Rodríguez-Ramos [1,2,*]

[1] Wooptix S.L., Av. Trinidad No. 61, 7, 38204 San Cristóbal de La Laguna, Spain; trujillo@wooptix.com
[2] Industrial Engineering Department, ESIT, Universidad de La Laguna, 38200 San Cristóbal de La Laguna, Spain
* Correspondence: kiril.ivanov.kurtev@wooptix.com (K.I.K.); jmramos@wooptix.com (J.M.R.-R.)

Abstract: In this work, we demonstrate the use of a chromatic confocal sensor for long-distance measurements. The sensor increases the working distance of state-of-the-art confocal sensors by a factor of 10, reaching a working distance of 620 mm. The chromatic aberration exhibited by a lens was utilized to establish the working range. The chromatic dispersion of the optics led to images of the different wavelength components at different longitudinal points along the optical axis. The sensor employs a robust algorithm to measure relative displacements of the sample's motion. The calibration process simplifies data analysis and improves the accuracy of displacement measurements in experimental setups. To facilitate the design process, a simulator was developed specifically for this purpose. The calibration data obtained in both the experimental and the simulated data show that the simulator was able to predict the sensitivity with an error of 5%. We also describe the effect on the sensitivity of oversampling the spectrum. In addition, the superiority of low-pass filtering over Gaussian fitting over the detected spectrum is shown.

Keywords: chromatic confocal sensor; long-distance sensor

check for updates

Citation: Kurtev, K.I.; Trujillo-Sevilla, J.M.; Rodríguez-Ramos, J.M. Long-Distance Measurements Using a Chromatic Confocal Sensor. *Appl. Sci.* **2024**, *14*, 9943. https://doi.org/10.3390/app14219943

Academic Editors: Detlef Kip and Paolo Prosposito

Received: 11 September 2024
Revised: 25 October 2024
Accepted: 29 October 2024
Published: 30 October 2024

Copyright: © 2024 by the authors. Licensee MDPI, Basel, Switzerland. This article is an open access article distributed under the terms and conditions of the Creative Commons Attribution (CC BY) license (https://creativecommons.org/licenses/by/4.0/).

1. Introduction

Accurate distance measurement is paramount in industrial settings, serving diverse applications such as manufacturing, optical metrology, robotics, and quality control. Various methods are available to measure distance and displacement, surface profiles, and vibrations [1]. The widely used methods for distance measurement include intensity-based sensors [2], triangulation sensors [3], time-of-flight sensors [4], confocal sensors [5–11], and interferometric sensors [12–14]. These techniques offer high precision, rapid response times, and non-contact measurement, enabling efficient and precise operations without direct interaction with the target.

Among the methods mentioned above, only interferometry and chromatic confocal sensors can achieve a precision finer than one micrometer, providing extremely high resolution measurements [1,6,12]. The main disadvantage of interferometric sensors is that they are susceptible to slight motion and vibration [15].

Chromatic confocal sensors can be divided into two types: monochromatic confocal sensors [16,17] and polychromatic confocal sensors [5–9,11]. Their functionality is based on the well-known confocal microscopy, in which the narrow light from an aperture is focused on the sample and the scattered or reflected light after passing a pinhole is detected by a sensor. By applying an aperture, the out-of-focus light is rejected and the maximum intensity is obtained from the image plane [18].

Monochromatic sensors use a single wavelength, primarily a laser, illuminating the target with a small spot, and the reflected beam is gathered through a pinhole. The object's surface profile is constructed by scanning the entire sample surface and obtaining the intensity of the spots. In contrast, the polychromatic sensor uses a broadband light source. The light is focused on the sample using a chromatic lens. The sensor collects the spectrum of the light reflected by the sample; provided that the spectrum profile changes accordingly to the distance to the sample, the change in distance from the sensor to the sample can

be related to changes in the spectrum's peak. Polychromatic sensors are devices for the accurate measurement of the depth and topography of an object, even when the object contains various materials and colors. Hu et al. [19] have developed a fast chromatic confocal sensor that is capable of working on different reflective surfaces. A similar work was done by Jeong et al. [20], in which they managed to measure the surface of non-specular reflective surfaces with an axial resolution of about 130 µm.

A key comparison in high-precision optical measurement lies between laser interferometry and confocal sensing, as both methods offer excellent resolution and working distance ratios, typically in the micrometer range [1]. Although laser interferometry can achieve a sub-nanometric resolution and accommodate larger working distances, confocal sensors present several advantages. Confocal sensing is more robust against vibrations, requires simpler calibration, and involves a less complex setup. Moreover, while this work primarily focuses on relative measurements, confocal sensors have the potential to provide absolute distance measurements by linking focus distances for different wavelengths with a calibration curve. In contrast, laser interferometry is generally more suited for displacement monitoring, rather than absolute distance measurement, making confocal sensing a versatile alternative in applications requiring precise distance tracking, such as industrial manufacturing [21].

Most works on confocal sensors in the recent literature have focused on working distances below 50 mm [22,23]. In this study, we present the development of a polychromatic confocal sensor that employs a robust algorithm to measure the relative displacement of the sample. The key advantage of this sensor, compared to conventional chromatic confocal sensors, is its ability to operate at longer working distances without altering the optical configuration of an existing industrial machine. This makes the sensor particularly suitable for applications involving the measurement of thickness and depth in extended samples through axial motion. Additionally, a Python-based simulator has been created to assist in the design process and predict the sensor's performance, with the source code available for public use.

2. Experimental Setup

The chromatic confocal sensor was purposefully designed to integrate into an existing optical setup for the wave front phase measurement of 300 mm diameter optics (Figure 1), developed in [24].

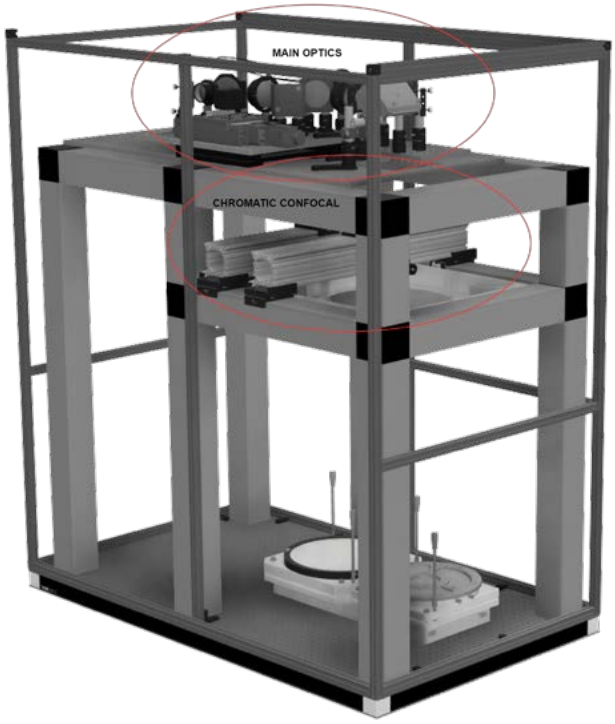


Figure 1. Phemet LabTool render.

The experimental setup is shown in Figure 2. The sensor can be split into four main components: illuminator, collector, signal conditioner, and spectrometer. The illuminator path consists of a Tungsten-Halogen Light Source (SLS201L, Thorlabs, Newton, NJ, USA), which delivers a consistent intensity spectrum of 10 mW black-body-like radiation, spanning from 360 to 2600 nm, coupled to a multimode 50 µm core optical fiber patch cable. The other end of the optical fiber is at the focal plane of a positive achromatic doublet lens of 100 mm focal length. The broadband collimated beam emerging from the collimator passes through a 50/50 non-polarizing beam splitter and finally is focused by a large singlet aspheric lens made of BK7 glass; the most relevant optical parameters are shown in Table 1. The singlet design of this lens causes a large focal shift between the extremes of the spectrum. The sample is typically placed at the midpoint of this range.

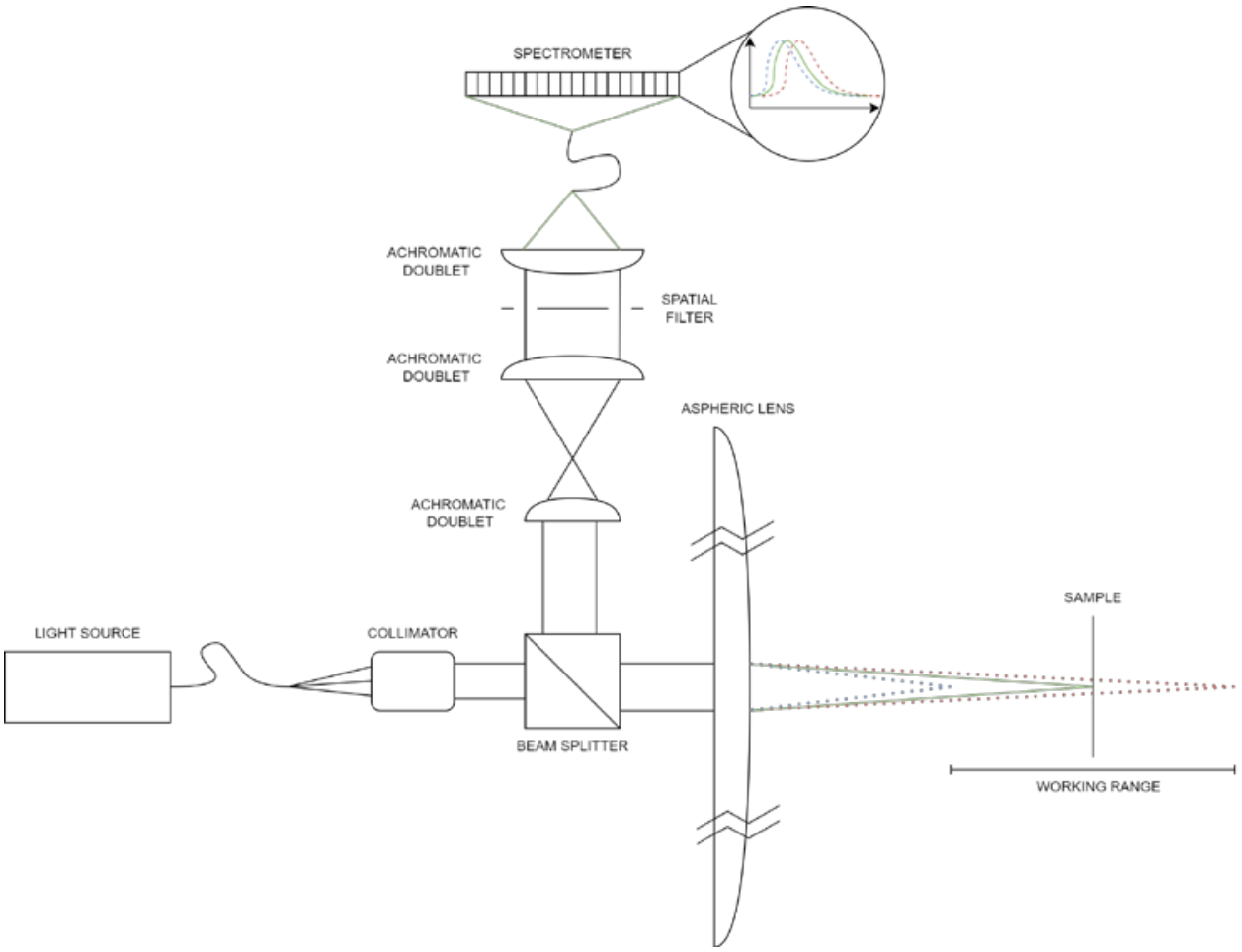


Figure 2. Full optical setup. Shorter wavelengths will focus closer to the dispersion lens (blue), while bigger wavelengths will focus farther (red).

The collector part starts when the light reflected by the sample is partially collimated by the aspheric singlet lens. Again, the singlet design of the lens produces a difference in the collimation of different wavelengths, i.e., the wavelength of the best collimation changes if the sample is moved closer or farther from the aspheric lens. The beam splitter directs the reflected light to an achromatic doublet of 30 mm focal length.

The signal conditioner is composed of three achromatic doublets, a spatial filter, and a pinhole. The first two achromatic doublets work as a Keplerian beam expander, expanding the beam to a diameter of 25 mm in order to enable the use of a spatial filter, blocking an inner disk of 20 mm in diameter. The last achromatic doublet lens focuses the filtered light into a 200 µm pinhole.

Table 1. Aspheric lens optical parameters.

Parameter	Value
Curvature	plano-convex
Radius	329.8 mm
Diameter	345 mm
Clear aperture	310 mm
Material	N-BK7
Conic	−0.604
Focal length (590 nm)	620 mm
Central thickness	60 mm

The spectrometer (CCS175, Newton, NJ, Thorlabs, USA) is coupled via a bundle fiber to the back of the pinhole. The spectral range is from 500 to 1000 nm with a resolution of 0.16 nm. The full chromatic confocal sensor assembly is shown in Figure 3.



Figure 3. Chromatic confocal sensor render.

Finally, the displacement of the sample towards the main lens results in a shift of the spectrum's maxima towards shorter wavelengths; a converse shift occurs when the sample is displaced further from the main lens.

Optical Performance

Several critical parameters for a chromatic confocal sensor include the working distance, the measurement range, the axial and lateral resolution, and the maximum tilt angle of the sample [11]. These parameters collectively determine the sensor's performance, impacting its versatility and suitability for various applications.

The working distance of our system corresponds to the effective focal length of the primary aspheric lens, measuring 620 mm for a wavelength of 590 nm. It is worth mentioning that even if the aspherical shape of the main lens is aimed to decrease the spherical aberration it does not remove entirely. Furthermore, the confocal sensor uses a small portion of the center of the lens, as shown in Figure 4, and so the focal lengths for different wavelengths will be larger than those given in the specifications of the lens. In Figure 5,

the focal lengths for the marginal rays of an incident light with a diameter of 25.4 mm are shown. In addition, it is important to note that the central rays of the collimated light incident on the main lens will have even higher focal lengths and extend the working range of the sensor even further, which is why the last optical relay was introduced, to magnify the collimated light after reflection on the sample and to introduce a spatial filter to block these rays (see Figure 6) and maintain the desired working range.

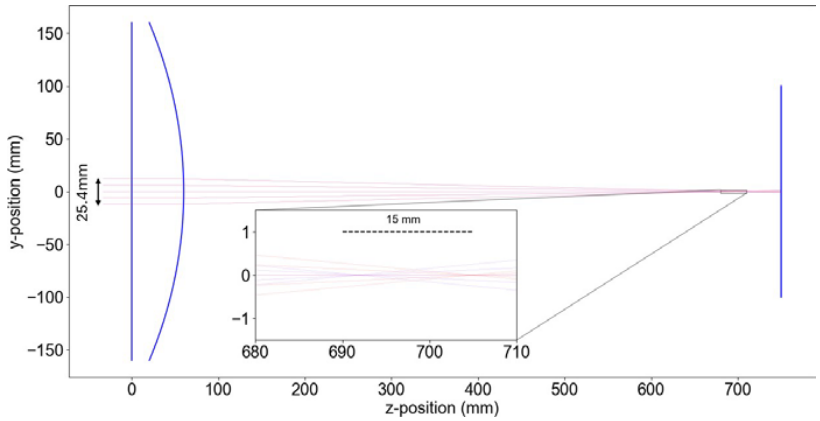


Figure 4. Theoretical working range given by the Python simulator.

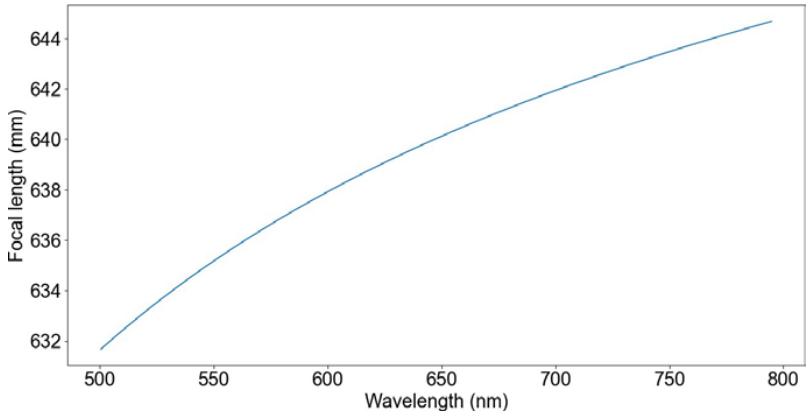


Figure 5. Focal lengths for different wavelengths for the main aspheric lens.

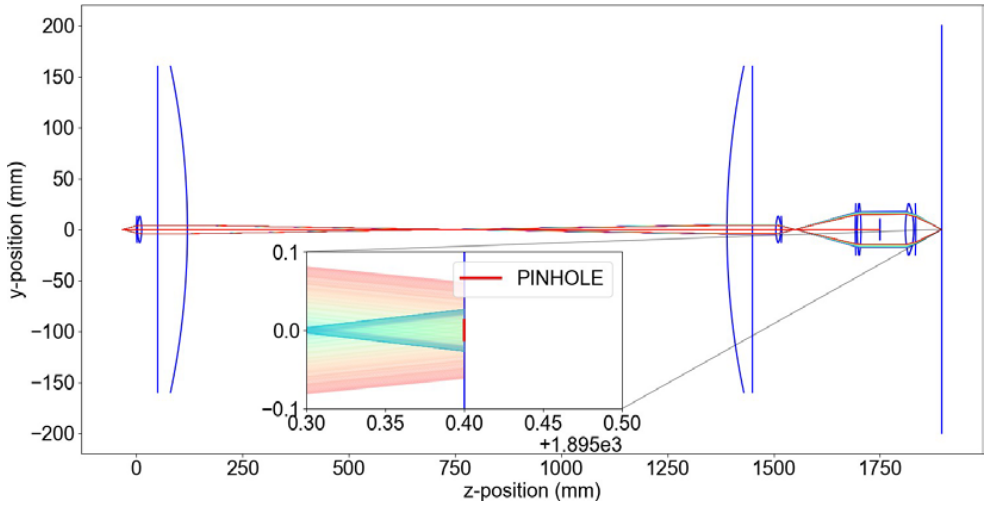


Figure 6. Setup plot from the developed Python module. Shorter wavelengths are shown in blue, while longer wavelengths are shown in red.

The measurement range is bounded by the extremes of the light source's wavelength spectrum, spanning from 550 nm to 1100 nm. However, our system is tailored to operate within a narrower spectral range, precisely from 550 to 800 nm, because of the antireflective coating used on all of the lenses. Theoretically, if the beam reaching the aspheric lens is perfectly collimated for all wavelengths, the measurement range of the sensor, given by the chromatic dispersion of the optics, will lead to images of the different wavelength components at different longitudinal points along the optical axis of around 15 mm. The exact value of the working range will be delimited by the spatial filter and also by the exact height at which the marginal ray hits the main lens. This value is given by the chromatic aberration of the main lens and also by the height of the marginal ray that comes from the collimator, as seen in Figure 4.

For the purpose of this work, which is to demonstrate the capability of the chromatic sensor to operate in a long-distance setup, the lateral resolution is not a primary concern. However, it remains influenced by the point spread function of the aspheric lens and the extent of the collimation of the light source. The axial resolution hinges mainly on the spectrometer's resolution and the chromatic aberration inherent in the optical setup. In a focused system, the axial and lateral resolution can be described by the radius of the diffraction of the Airy disk in the lateral (x, y) image plane, as defined in Equation (1); the equivalent of this in the axial direction is given by Equation (2).

$$\text{Abbe Resolution}_{x,y} = \frac{\lambda}{2NA} \approx 1.5\ \mu\text{m} \tag{1}$$

$$\text{Abbe Resolution}_{z} = \frac{2\lambda}{NA^2} \approx 18\ \mu\text{m} \tag{2}$$

Finally, the maximum permissible tilt of the sample is determined by the diameter of the collimated light source and the aperture of the optical element succeeding the main lens, as illustrated in Figure 7. This maximum tilt angle is calculated as follows, producing a value of 0.38° for the configuration shown in the previous section.

$$\tan(\theta + \varphi) = \tan(2\varphi + \phi) = \frac{d}{f} \tag{3}$$

$$\tan(\phi) = \frac{p}{f} \tag{4}$$

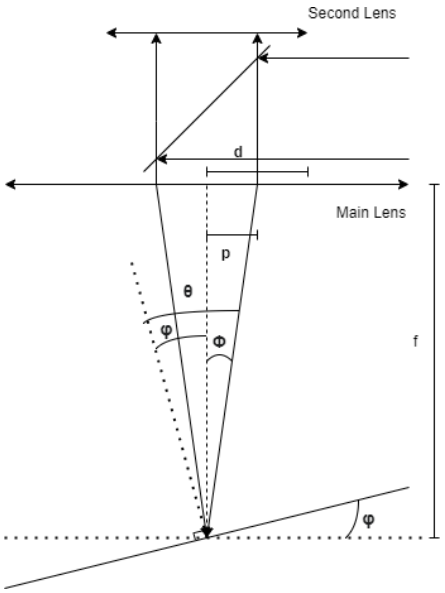


Figure 7. Maximum tilt angle for the sample.

3. Simulator Software

To facilitate the design of the chromatic confocal sensor, a custom Python module was developed specifically for this purpose. Simulations were conducted considering the actual surfaces of the experimental setup. This module offers a straightforward approach to optical design for the chromatic confocal sensor; it would also help other authors to develop their own sensors, provided the open-source nature of the software. Figure 6 illustrates the optical design along with ray tracing for the minimum and maximum wavelengths utilized in the experiment. Due to the design specifications of the optical setup, including the beam splitter and achromatic lenses, the simulations were limited to a spectrum of up to 800 nm, as the system was optimized for wavelengths ranging from 300 to 800 nm.

To simulate the propagation of light rays through an aspheric optical system, we developed a ray-tracing module using Python 3.12. This module leverages numerical optimization techniques and performance enhancements to accurately model ray interactions with complex lens surfaces. The core of the simulation is based on solving for the intersection points between light rays and the surfaces of aspheric lenses, as well as computing the subsequent refraction according to Snell's law. All of the lenses are defined as aspheric surfaces. Those that are not aspheric will have the conic constant set to zero. The simulation workflow is detailed as follows:

3.1. Ray–Surface Intersection

The surfaces of the aspheric lenses are defined by the following conic equation:

$$z(y) = \frac{y^2}{R\left(1 + \sqrt{1 - (1+k)\left(\frac{y}{R}\right)^2}\right)} + z_0 \tag{5}$$

where R is the radius of curvature, k is the conic constant, and z_0 is the offset of the surface. To find the intersection of a ray with this surface, a merit function was constructed to describe the geometry of the ray relative to the surface. The system of equations is solved numerically using the *fsolve* from a Python scientific package called scipy [25], which is based on the Powell's minimization routine [26]. The solver computes the ray's coordinates (y, z) at the point of intersection with the lens, ensuring the geometric consistency between the ray's path and the surface.

3.2. Surface Slope and Refraction

Once the ray crosses the lens surface, the surface slope at the intersection point is computed using the derivative of the surface equation. This slope is necessary to determine the tangent to the surface, which, in turn, is used to compute the angle of incidence. The refraction on the lens surface is modeled using Snell's law:

3.3. Simulation Workflow

The overall simulation workflow involves:

- Generating an array of rays, either randomly or uniformly distributed across the light source radius.
- The iterative calculation of the intersection points of each ray with each optical surface.
- Updating the ray's trajectory, based on the calculated intersection and refraction.
- The storing of the traced rays for further analysis.

Using numerical optimization and efficient computational techniques, this module enables the simulation of complex optical systems, making it suitable for applications in chromatic confocal systems and other optical designs.

$$\sin(\theta_2) = \frac{n_1}{n_2}\sin(\theta_1) \tag{6}$$

where n_1 and n_2 are the refractive indices of the incident and refractive media, respectively, and θ_1 and θ_2 are the angles of incidence and refraction. The refracted angle is then used to update the trajectory of the ray as it propagates through the lens.

3.4. Ray Tracing Through Optical Elements

The simulation handles multiple optical elements by iterating through all surfaces in the system. Rays are initialized at the light source, and their propagation is traced through successive elements. The refractive index of each element is obtained from a pre-defined dataset in a JSON-like file, and the ray's intersection and refraction are recalculated at each surface.

The software can be used freely as a Python module and can be found at [27]. All simulations were carried out using version 0.1.34.

4. Methods

The methodology entails leveraging the chromatic aberration exhibited by a lens to establish a working range, given by the focal lengths, corresponding to different wavelengths. The illumination of the primary lens with a collimated white-light beam generates this working range.

Figure 8 shows two spectra that were captured at two separate positions of the sample, separated by 800 µm. Even though the spectrum has changed, the maximum value lies in the same wavelength, thus demonstrating that the detection of the peak wavelength in a raw spectrum signal is not enough even to resolve a large distance. To mitigate this issue, two distinct methods were employed: low-pass filtering and Gaussian fitting.

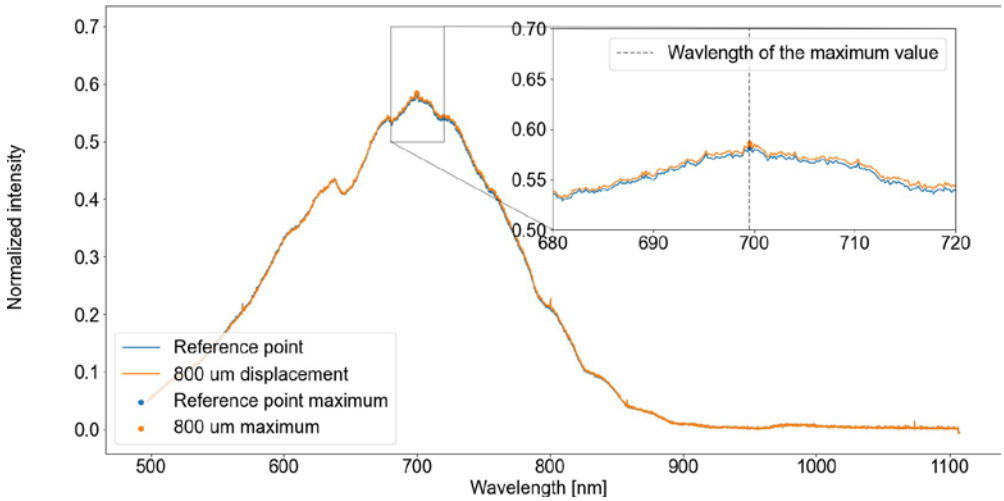


Figure 8. Two captured spectra for different sample positions.

4.1. Low-Pass Filtering Method

The low-pass filtering method involves isolating and retaining only the lowest frequency components of the spectrum. This process is achieved by performing a Discrete Fourier Transform (DFT) on the detected spectral signal, as outlined in Equation (7). The DFT converts the spectral data from the time (or wavelength) domain into the frequency domain, enabling the separation of different frequency components. Mathematically, the DFT of a discrete signal $S(n)$ is given by

$$X(k) = \sum_{n=0}^{N-1} S(n) \cdot e^{-i2\pi \frac{k}{N} n} \tag{7}$$

where $S(n)$ represents the sampled spectrum, N is the number of data points in the spectrum, and $X(k)$ are the frequency-domain coefficients, each corresponding to a specific frequency

component of the signal. These coefficients indicate the contribution of various frequency components to the overall spectral data.

After applying the DFT, a rectangular low-pass filter is employed in the frequency domain to remove higher-frequency components and retain only the low-frequency parts of the signal. This filter essentially "cuts off" frequencies above a certain threshold, passing only those below it. Mathematically, the rectangular filter $H(k)$ can be defined as

$$H(k) = \begin{cases} 1 \text{ if } |k| \leq k_{\text{cutoff}} \\ 0 \text{ if } |k| > k_{\text{cutoff}} \end{cases} \quad (8)$$

where k_{cutoff} is the cutoff frequency defining the boundary between the low and high frequencies. The filtered signal $X_{filtered}(k)$ is then obtained by multiplying the DFT coefficients $X(k)$ by the filter $H(k)$:

$$X_{\text{filtered}}\ (k) = X(k) \cdot H(k) \quad (9)$$

By performing the inverse DFT (IDFT) on the filtered frequency components, the signal is transformed back into wavelength domain. The resulting signal now contains only the smooth, slowly varying features, which correspond to the low-frequency components of the original spectrum.

In Figure 9, the impact of applying low-pass filtering on the spectrum is illustrated. Notably, the maximum intensity value, which originally corresponded to a distinct peak in the unfiltered spectrum, no longer aligns precisely after filtering. The resulting spectrum is smoother, making it easier to track gradual variations in the signal, such as those caused by sample displacement.

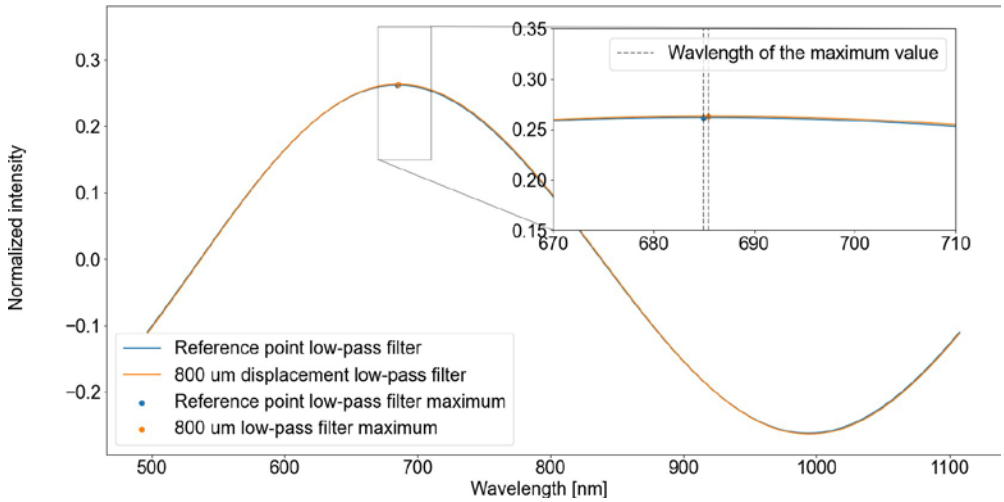


Figure 9. Two captured spectra for different sample positions after low-pass filtering.

4.2. Gaussian Fitting Method

A similar approach was employed to fit a Gaussian distribution to the averaged spectral data. This fitting process was executed using a nonlinear, least-squares optimization method, as outlined in [28]. Specifically, the nonlinear regression technique was utilized to estimate the parameters $\theta = \{\mu, \sigma, A\}$, where one symbol is the mean (or peak location), another symbol is the standard deviation (which defines the width of the Gaussian), and A is the amplitude of the distribution. The objective is to minimize the residual sum of squares between the observed spectral data points, y_i, and the predicted values of the Gaussian model $f\ (x_i, \theta)$, formalized in the cost function

$$S(\boldsymbol{\theta}) = \sum_{i=1}^{n} [f(\boldsymbol{\theta}; \mathbf{x_i}) - y_i]^2 \quad (10)$$

where $f\ (x_i, \theta)$ represents the Gaussian function, typically given by

$$f(x) = \frac{1}{\sigma\sqrt{2\pi}} e^{-\frac{1}{2}\left(\frac{x-\mu}{\sigma}\right)^2} \tag{11}$$

The nonlinear least-squares fitting process aims to iteratively adjust the parameter set, θ, to minimize the difference between the model and the measured data points. This is typically achieved using optimization algorithms, such as method- or gradient-based techniques, which are well suited for problems involving nonlinearities in the parameter space. The optimal parameter values correspond to the best-fit Gaussian distribution that characterizes the averaged spectra. This allows for the critical properties of the spectra, such as the peak location (i.e., the maximum of the distribution given by μ), to be precisely tracked. Monitoring these properties is essential for understanding spectral shifts.

4.3. Spectrum Oversampling

In Figure 10, the impact of a displacement of 800 µm on the spectrum is demonstrated, where the peak of the distribution shifts by 0.498 nm. Given the resolution of the spectrometer, which is 0.16 nm, this spectral shift results in a calculated displacement sensitivity of approximately 250 µm. However, this sensitivity is constrained by the intrinsic resolution limit of the spectrometer, defined by the smallest wavelength interval it can reliably detect. To enhance the sensitivity and improve the precision of the displacement detection, the detected spectrum can be oversampled. This technique effectively increases the apparent resolution of the spectrometer, allowing for finer distinctions between spectral peaks. The oversampling process is achieved by linear interpolation between the actual data points obtained from the spectrometer. Linear interpolation works by estimating the values between the discrete data points that are directly measured by the spectrometer. If the spectrometer measures at wavelengths λ_i and λ_{i+1}, linear interpolation constructs intermediate values, based on the assumption that the data between these points vary linearly. Mathematically, for a given point, λk, between λ_i and λ_{i+1}, the interpolated value S(λk) of the spectrum can be estimated as

$$S(\lambda_k) = S(\lambda_i) + \frac{S(\lambda_{i+1}) - S(\lambda_i)}{\lambda_{i+1} - \lambda_i} \cdot (\lambda_k - \lambda_i) \tag{12}$$

where $S(\lambda_i)$ and S(λ_{i+1}) represent the spectrum intensities at the measured wavelengths λ_i and λ_{i+1}, respectively, and λk is the new interpolated wavelength. By performing this interpolation across the entire spectral range, additional virtual data points are created, effectively refining the wavelength resolution beyond the hardware limitations of the spectrometer.

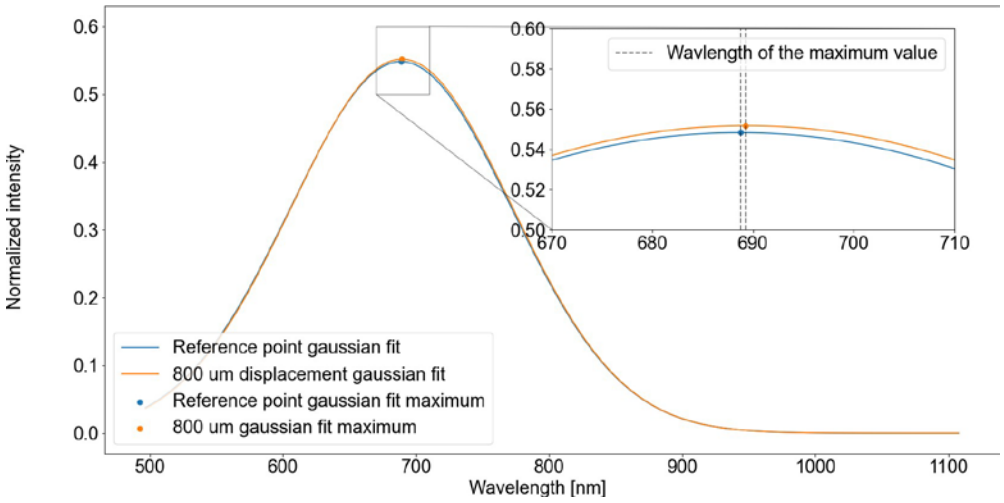


Figure 10. Two captured spectra for different sample positions after Gaussian fitting.

The result of oversampling is a denser spectrum with more closely spaced data points, allowing for a more precise determination of the spectral peak position and improved sensitivity in detecting small displacements. This is particularly beneficial in applications where sub-nanometer shifts in the spectrum need to be detected but the physical resolution of the spectrometer is insufficient.

5. Calibration

To enhance the quality of the measurements, the chromatic confocal sensor must be calibrated by establishing a calibration curve. This calibration curve serves as a reference standard, enabling the straightforward tracking of sample displacement by correlating spectral changes with known displacements.

The calibration procedure consisted of mounting a 50 mm diameter flat mirror on a linear translation stage. The sample was positioned at 620 mm from the aspheric lens, and a total distance of 800 µm was scanned with a step size of 20 µm.

The experiment was carried out in a dark room environment, and the exposure time was set to 200 ms to ensure the optimal conditions for measurement accuracy. To increase the repeatability of the measurement, 3000 spectra were acquired for each sample position. These displacements were carried out in the direction opposite to the lens, resulting in the anticipated movement of tracked peaks towards longer wavelengths.

This calibration step also works as a validation of the provided simulator software; for this, we simulated the same setup used for calibration. The comparison of calibration curves, both experimental and simulated, reveals a similarity, as depicted in Figure 11, and Table 2 provides a comparison of the slopes of both curves, indicating an estimated difference of 5%. It is important to note that the simulated spectra exhibit an infinite signal-to-noise ratio (SNR), and the extent of the light source is negligible; the spectral resolution was down-sampled by a factor of five, and the number of rays used was 220,000, suggesting potential areas for simulation enhancement. However, these findings suggest that the module serves as a reliable initial step in the design of a chromatic confocal sensor.

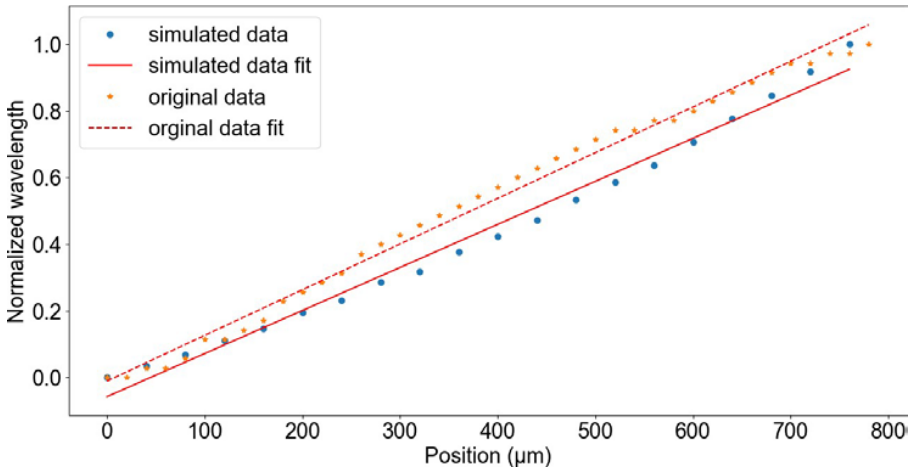


Figure 11. Two calibration lines: simulated (blue) and experimental (orange).

Table 2. Parameters of fitter lines over real and experimental data.

	Slope	R-Squared
Simulated	0.00129	0.994
Real	0.00137	0.996

The discrepancy between the real and simulated data, apart from those mentioned above, is mainly due to the position of the sample inside the working range. As shown

in Figure 5, we can clearly see that the spacing between the foci of shorter wavelengths is bigger than the spacing between the ones of higher wavelengths. Furthermore, it is worth noting that if we are in the range of higher wavelengths and if we go through a sufficiently small range, we can approximate the calibration curve to a straight line.

Moreover, the wavelengths are normalized because the detected peak wavelength does not match the one in the real data, which is due to the coatings of the lenses, which will strongly affect the transmitted intensity of each wavelength and, therefore, the detected wavelength peak, and it is not considered in the simulation.

Lastly, we only aimed at the region where the biggest sensitivity had been achieved experimentally. Furthermore, the motive of this work was to measure the thickness of a silicon wafer from a long distance. The thickness of a single wafer is around 775 µm, which is the reason for the small range of 800 µm being used inside the working range.

6. Results

In this section, we will show the effect of applying the different proposed methods to increase the sensitivity of the sensor.

Each displacement was executed in increments of 20 µm. At each position, three thousand spectra were captured, and the averages of each one hundred spectra were computed to enhance the signal-to-noise ratio (SNR), resulting in thirty spectra per displacement. In Figure 12, the standard deviation (STD) for each sample position, based on 30 captured spectra, is compared. The upper section of the figure illustrates that the Gaussian fit generally exhibits a higher STD value across most of the sample positions, with the exception of two. The lower section displays the result of subtracting the frequency filter curve from the Gaussian fit curve. This difference shows that, apart from two sample positions, the values are predominantly positive, indicating that the uncertainty associated with the Gaussian fit is, on average, greater than that of the frequency filter within the examined range. The "Gaussian fit with 10 interpolated points" are scattered points, since some standard deviation values had a value of zero as no peak movement was detected, which is the same effect that is illustrated in Figure 8. The mean standard deviation with the largest oversampling outperforms the one with fewer interpolated points by a factor of 3.8.

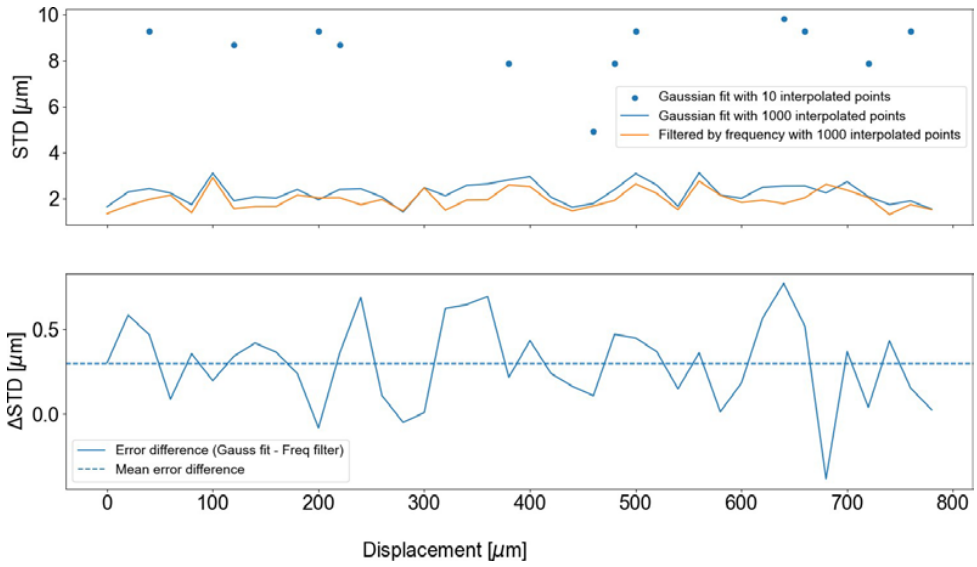


Figure 12. A standard deviation comparison between the low-pass filtering (with no interpolation and interpolation) and the Gaussian fit for each measurement.

To justify the number of interpolated points, in Section 4.3, the actual resolution of 250 µm/nm was obtained experimentally, supposing a linear shift between the detected peaks. Thus, in order to be able to detect movements of 20 µm, at least 10 more values need

to be interpolated to allow the peak detection for such sample displacements. The higher value of 1000 interpolated points was motivated by the highest spectrometer's resolution that can be found commercially, which is in the order of picometers.

Additionally, an interpolation between real spectrum values was performed; for Figure 13, the resolution was enhanced by a factor of ten, while for Figure 14, the resolution was increased by a factor of 1000, yielding a significantly higher resolution than the original results. Therefore, as previously stated, this interpolation step is crucial when the spectrometer's resolution is insufficient to achieve the desired axial resolution.

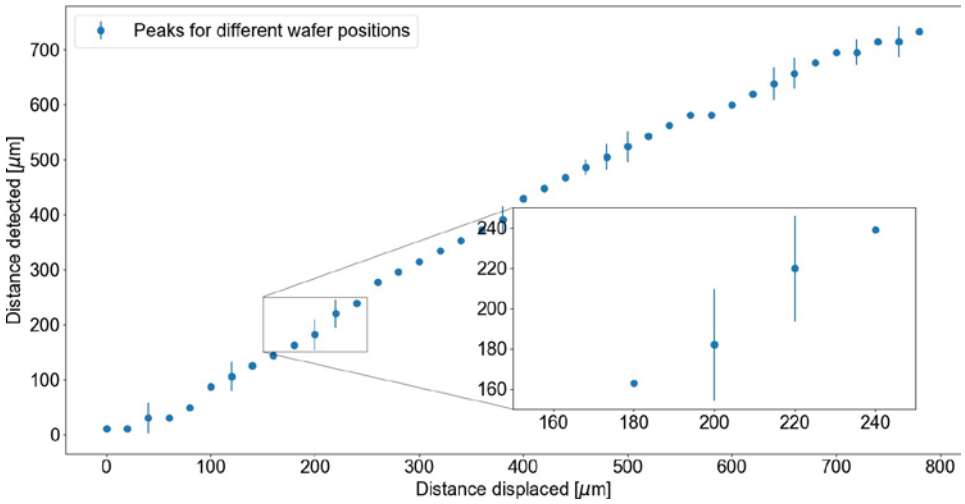


Figure 13. Distance measured vs. distance displaced with 10 interpolated points between real spectrum values. Error bars show three standard deviations.

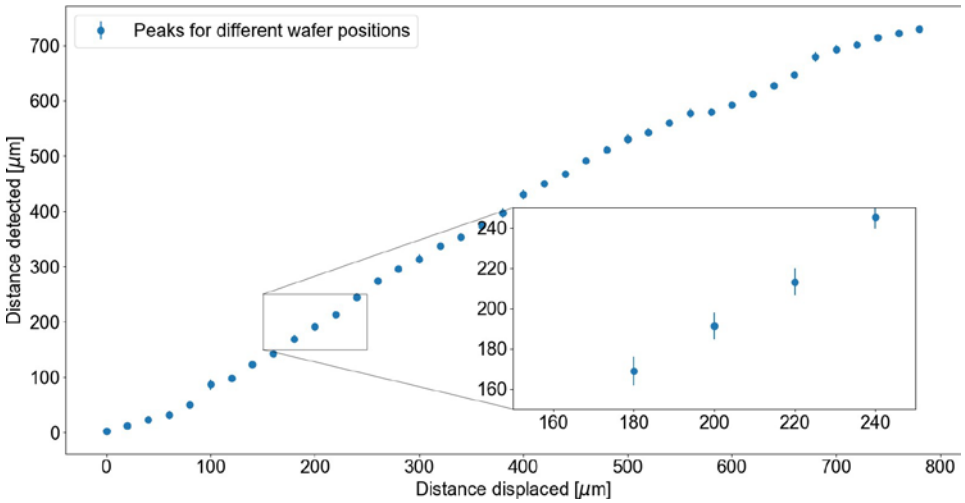


Figure 14. Distance measured vs. distance displaced with 1000 interpolated points between real spectrum values. Error bars show three standard deviations.

7. Conclusions

In conclusion, our study demonstrates the practicality and effectiveness of integrating a chromatic confocal sensor into a fixed optical setup, emphasizing the optimization of both the illumination and the sensing components. By carefully selecting and calibrating the chromatic lenses, we achieved a 20-micrometer resolution over a significant distance of 620 mm, highlighting the system's adaptability for various applications. The development of a custom Python module further streamlined the sensor design process, eliminating the need for expensive commercial software. However, our experiments revealed an error margin of approximately 5% compared to the real data, underlining the importance of validating simulation results with empirical testing.

Our findings also show that oversampling effectively enhances the axial resolution without the need for high-resolution spectrometers, and low-pass filtering outperforms Gaus sian fitting in peak detection. Looking ahead, we aim to optimize the extension of the light source fiber optic output to minimize the spot size and further improve the axial resolution. Additionally, we will explore the use of positive and negative lenses to address the challenges associated with the wide measurement range of the primary chromatic lens. Furthermore, in long-distance measurements, environmental factors are crucial for obtaining reliable and accurate data. In the present work, these factors were not studied since the experiment was carried out in a temperature-controlled environment (less than 0.5 °C temperature variation).

The current device has demonstrated its capability to measure the thickness of reflective samples, such as silicon wafers, and to track relative displacements. With proper calibration and the use of calibration curves, absolute distance measurements can also be achieved. By extending the working distance of chromatic confocal sensors from the typical range of hundreds of micrometers to tens of millimeters, as described by Berkovic et al. [1], to around 600 mm, our method broadens the scope of applications for these sensors.

Typically, confocal sensing offers the advantage of a wavelength versus distance response that is independent of the object's properties, whether reflective, diffuse, light, or dark. However, in our current work, the long working distance introduces challenges, such as a reduced sensitivity to low-reflectivity or diffuse surfaces. Although low reflectivity can be compensated by increasing exposure times, diffuse surfaces remain difficult to measure and would be an interesting subject for future characterization.

The resolution is primarily influenced by three factors: noise in the light spectrum, meaning that a flat spectrum would ideally be preferable; spectrometer readout noise, which can be minimized by increasing the exposure times, an approach we attempted; and, most critically, the dispersion range of the main lens. These factors collectively impact the precision of the measurements. As discussed earlier, increasing the number of interpolation points between the real data reduces the positional uncertainty, as shown by the error bars in Figures 13 and 14, representing the standard deviation at each sample position. Thus, increasing the interpolation points infinitely will not increase the sensor's resolution further. These are physical limitations.

Another limitation is the system's small tip/tilt tolerance of 0.38°, which could easily be addressed by incorporating a tip/tilt stage to correct the sample orientation. This was not a primary focus of our study, as we concentrated on highly reflective and flat surfaces, such as silicon wafers and mirrors. However, future experiments could explore the sensor's performance with varying sample orientations and more complex surface types.

These advances offer significant potential for enhancing chromatic confocal sensor capabilities in various fields, where long-distance measurements with high accuracy are crucial, ranging from manufacturing to metrology. This paves the way for greater precision and reliability in measurement and imaging tasks.

Author Contributions: Conceptualization, J.M.T.-S.; Methodology, J.M.T.-S.; Software, K.I.K.; Investigation, K.I.K.; Writing—original draft, K.I.K.; Supervision, J.M.T.-S. and J.M.R.-R.; Funding acquisition, J.M.R.-R. All authors have read and agreed to the published version of the manuscript.

Funding: This research received no external funding.

Institutional Review Board Statement: Not applicable.

Informed Consent Statement: Not applicable.

Data Availability Statement: The raw data supporting the conclusions of this article will be made available by the authors on request.

Conflicts of Interest: Authors Kiril Ivanov Kurtev, Juan Manuel Trujillo-Sevilla and José Manuel Rodríguez-Ramos were employed by the company Wooptix S.L. The remaining authors declare that the research was conducted in the absence of any commercial or financial relationships that could be construed as a potential conflict of interest.

References

1. Berkovic, G.; Shafir, E. Optical methods for distance and displacement measurements. *Adv. Opt. Photon.* **2012**, *4*, 441–471. [CrossRef]
2. Shen, W.; Wu, X.; Meng, H.; Zhang, G.; Huang, X. Long distance fiber-optic displacement sensor based on fiber collimator. *Rev. Sci. Instrum.* **2010**, *81*, 123104. [CrossRef] [PubMed]
3. Ji, Z.; Leu, M.C. Design of optical triangulation devices. *Opt. Laser Technol.* **1989**, *21*, 339–341. [CrossRef]
4. Massa, J.S.; Buller, G.S.; Walker, A.C.; Cova, S.; Umasuthan, M.; Wallace, A.M. Time-of-flight optical ranging system based on time-correlated single-photon counting. *Appl. Opt.* **1998**, *37*, 7298–7304. [CrossRef]
5. Miks, A.; Novak, J.; Novak, P. Analysis of method for measuring thickness of plane-parallel plates and lenses using chromatic confocal sensor. *Appl. Opt.* **2010**, *49*, 3259–3264. [CrossRef]
6. Wei, H.; Wang, W.; Wang, X.; Li, Y. Bullet signature measurement with chromatic confocal sensor. *Appl. Opt.* **2020**, *59*, 6594–6599. [CrossRef]
7. Bai, J.; Li, X.; Zhou, Q.; Ni, K.; Wang, X. Improved chromatic confocal displacement-sensor based on a spatial-bandpass-filter and an X-shaped fiber-coupler. *Opt. Express* **2019**, *27*, 10961–10973. [CrossRef]
8. Wang, X.; Ma, T. Chromatic confocal sensor with dual dispersion for extending the measuring range. *Proc. SPIE* **2021**, *12072*. [CrossRef]
9. Liu, C.; Lu, G.; Liu, C.; Li, D. Compact chromatic confocal sensor for displacement and thickness measurements. *Meas. Sci. Technol.* **2023**, *34*, 055104. [CrossRef]
10. Sanchez-Ortiga, E. Scanning microscopy with spatial sampling of the detector plane. *Opt. Pura y Apl.* **2013**, *46*, 137–146. [CrossRef]
11. Hillenbrand, M.; Mitschunas, B.; Wenzel, C.; Grewe, A.; Ma, X.; Feßer, P.; Bichra, M.; Sinzinger, S. Hybrid hyperchromats for chromatic confocal sensor systems. *Adv. Opt. Technol.* **2012**, *1*, 187–194. [CrossRef]
12. Koch, A.; Ulrich, R. Fiber-optic displacement sensor with 0.02 m resolution by white-light interferometry. *Sens. Actuators A Phys.* **1990**, *25*, 201–207. [CrossRef]
13. Shang, H.T. Chromatic dispersion measurement by white-light interferometry on metre-length single-mode optical fibres. *Electron. Lett.* **1981**, *17*, 603–605. [CrossRef]
14. Behrends, G.; Stöbener, D.; Fischer, A. Integrated, Speckle-Based Displacement Measurement for Lateral Scanning White Light Interferometry. *Sensors* **2021**, *21*, 2486. [CrossRef]
15. Yang, S.; Zhang, G. A review of interferometry for geometric measurement. *Meas. Sci. Technol.* **2018**, *29*, 102001. [CrossRef]
16. Yang, L.; Wang, G.; Wang, J.; Xu, Z. Surface profilometry with a fibre optical confocal scanning microscope. *Meas. Sci. Technol.* **2000**, *11*, 1786. [CrossRef]
17. Kim, C.S.; Yoo, H. Three-dimensional confocal reflectance microscopy for surface metrology. *Meas. Sci. Technol.* **2021**, *32*, 102002. [CrossRef]
18. Huang, Y.; Zhang, K.; Lin, N.; Kang, J.U. A Motion Compensated Fiber Optic Confocal Microscope based on Common-path Optical Coherent Tomography Distance Sensor. In *Optical Fibers, Sensors, and Devices for Biomedical Diagnostics and Treatment XI*; SPIE: Bellingham, WA, USA, 2011; Volume 50.
19. Hu, H.; Mei, S.; Fan, L.; Wang, H. A line-scanning chromatic confocal sensor for three-dimensional profile measurement on highly reflective materials. *Rev. Sci. Instrum.* **2021**, *92*, 053707. [CrossRef]
20. Jeong, D.; Park, S.J.; Jang, H.; Kim, H.; Kim, J.; Kim, C.S. Swept-Source-Based Chromatic Confocal Microscopy. *Sensors* **2020**, *20*, 7347. [CrossRef]
21. Li, J.; Ma, R.; Bai, J. High-Precision Chromatic Confocal Technologies: A Review. *Micromachines* **2024**, *15*, 1224. [CrossRef]
22. Yang, W.; Du, J.; Qi, M.; Yan, J.; Cheng, M.; Zhang, Z. Design of Optical System for Ultra-Large Range Line-Sweep Spectral Confocal Displacement Sensor. *Sensors* **2024**, *24*, 723. [CrossRef] [PubMed]
23. He, N.; Hu, H.; Cui, Z.; Xu, X.; Zhou, D.; Chen, Y.; Gong, P.; Chen, Y.; Kuang, C. Compact Chromatic Confocal Lens with Large Measurement Range. *Sensors* **2024**, *24*, 5122. [CrossRef] [PubMed]
24. Trujillo-Sevilla, J.M.; Rodríguez-Ramos, J.M.; Gaudestad, J.O.; Osterheld, T.; Cherian, B.; Brown, B. New metrology technique for measuring patterned wafer geometry on a full 300mm wafer. In *Proceedings of the Metrology, Inspection, and Process Control XXXVI*; SPIE: Bellingham, WA, USA, 2022; Volume 12053, pp. 6–12.
25. Virtanen, P.; Gommers, R.; Oliphant, T.E.; Haberland, M.; Reddy, T.; Cournapeau, D.; Burovski, E.; Peterson, P.; Weckesser, W.; Bright, J.; et al. SciPy 1.0: Fundamental Algorithms for Scientific Computing in Python. *Nat. Methods* **2020**, *17*, 261–272. [CrossRef]
26. Powell, M.J. A new algorithm for unconstrained optimization. In *Nonlinear Programming*; Elsevier: Amsterdam, The Netherlands, 1970; pp. 31–65.
27. Kurtev, K.I. Chromatic Confocal Sensor Ray Tracer. 2024. Available online: https://pypi.org/project/confocal-raytracer/ (accessed on 10 September 2024).
28. Vugrin, K.W.; Swiler, L.P.; Roberts, R.M.; Stucky-Mack, N.J.; Sullivan, S.P. Confidence region estimation techniques for nonlinear regression in groundwater flow: Three case studies. *Water Resour. Res.* **2007**, *43*, W03423. [CrossRef]

Disclaimer/Publisher's Note: The statements, opinions and data contained in all publications are solely those of the individual author(s) and contributor(s) and not of MDPI and/or the editor(s). MDPI and/or the editor(s) disclaim responsibility for any injury to people or property resulting from any ideas, methods, instructions or products referred to in the content.